3D gradient coil design for open MRI systems

Peter T. While [a,*], Larry K. Forbes [a], Stuart Crozier [b]

[a] School of Mathematics & Physics, University of Tasmania, Private Bag 37, Hobart, Tasmania 7001, Australia
[b] School of Information Technology & Electrical Engineering, University of Queensland, St. Lucia, Brisbane, Queensland 4072, Australia

ARTICLE INFO

ABSTRACT

Existing gradient coil design methods typically require some predetermined surface to be specified upon which the precise locations of coil windings are optimised with respect to gradient homogeneity and other measures of coil performance. In contrast, in this paper an analytic inverse method is presented for the theoretical design of 3D gradient coils in which the precise 3D geometry of the coils is obtained as part of the optimisation process. This method has been described previously for cylindrical whole-body gradients and is extended here for open MRI systems. A 3D current density solution is obtained using Fourier series combined with Tikhonov regularisation. The examples presented involve a minimum power penalty function and an optional shielding constraint. A discretised set of 3D coil windings is obtained using an equi-flux streamline seeding method. Results for an unshielded example display a concentration of windings within the portion of the coil volume nearest the imaging region and looped return path windings taken away from this region. However, for a shielded example the coil windings are found to lie almost exclusively on biplanar surfaces, suggesting that this is the optimum geometry for a shielded minimum power open coil.

1. Introduction

Gradient coils are principle components of magnetic resonance imaging (MRI) scanners and are used to spatially frequency-encode the region to be imaged by creating precise linear magnetic fields in three orthogonal directions (see for example, [1]). High image quality and short scan time demand strong gradient fields and rapidly switched coil currents. As such, primary design criteria include high gradient homogeneity, high coil efficiency and low coil inductance [2]. However, many secondary concerns impinge upon the advancement of gradient coil technology, such as eddy current induction, peripheral nerve stimulation, acoustic noise, and thermal heating (see for example, [3]). Gradient coil design has therefore received much attention and development over the last thirty years in the pursuit of optimizing these design criteria or arriving at optimum trade-offs for particular applications.

One branch of design methods of considerable note is that comprising the many extensions and variations to the target-field method of Turner [4]. In its original form, field quantities are expressed in terms of a Fourier-Bessel expansion and a current density solution is obtained on a cylinder of infinite extent using Fourier transforms. Constrained minimisation may be included in the method to obtain gradient coils displaying, for example, minimum power or inductance [2,5]. To obtain finite length coils, approximate filtering techniques in Fourier space may be used or the coil length may be constrained explicitly [6]. Alternatively, finite coil length may be imposed, for example, by representing the current density using Fourier series [7]. A Fourier series representation was combined successfully with Tikhonov regularisation by Forbes and Crozier [8–10] to solve an ill-posed integral equation and obtain finite length gradient and shim coils without approximation.

The analytic design methods discussed thus far tend to be restricted to geometries that display some level of symmetry and traditionally these are chosen to be either cylinders or parallel plates. Biplanar gradient coils can be used in open MRI systems, which are designed to help alleviate patient claustrophobia and to improve patient access for clinicians [11,12]. Applications of the target field method and constrained minimisation for this gradient coil structure are numerous (see for example, [13–15]). Additionally, coils of finite extent may be obtained by considering, for example, Fourier series representation for the current density [16–19]. Alternatively, it is also possible to design both cylindrical and biplanar gradient coil sets using coil-space optimisation strategies such as simulated annealing (see for example, [20–22]).

With the advancement in computer processing power, matrix inversion optimisation techniques combined with boundary element method type representations of the current surface have gained increasing popularity (see for example, [23–26]). The benefit of these methods is that once a suitable mesh has been generated, they are applicable to surfaces of arbitrary geometry

* Corresponding author. Tel.: +613 62262439; fax: +613 62262410.
E-mail address: pwhile@utas.edu.au (P.T. While).

[27,28]. In addition, they enable intricate physical processes, such as eddy current induction, to be modelled in a relatively straight-forward, albeit approximate and computationally intensive, manner (see for example, [29]). Analytic design methods nevertheless continue to be of great value, however, due to the rapid computation, tractability and physical insight they provide.

The exploration of alternative geometries to cylindrical or biplanar structures for gradient coils has become the subject of much recent work. Typically, the intention is to obtain coils that either offer a better coverage of the imaging volume or ameliorate one of the many secondary concerns in gradient operation listed above. For example, many novel geometries have been investigated in an attempt to reduce the very considerable acoustic noise generated as a result of large Lorentz forces induced within the coil (see for example, [30,31]), or to reduce the likelihood of peripheral nerve stimulation (see for example, [32]). Sanchez et al. [33] present an elegant method involving fuzzy membership functions followed by optimising adjustments to coil windings in 3D solution space to obtain dedicated gradient coils for breast imaging. In addition, many design methods include conical sections that link primary and shield current surfaces to redistribute return path windings and improve coil efficiency (see for example, [34–38]).

One feature common to the design methods discussed above is that some underlying physical structure must be chosen prior to implementation of the optimisation strategy. In contrast, While et al. [39] present an analytic 3D gradient coil design method in which the precise 3D geometry of the coil windings is found as part of the optimisation process. Fourier series are used to represent a 3D volumetric current density within a cylindrical volume surrounding the region of interest and an ill-conditioned integral equation related to minimum field error is solved using Tikhonov regularisation and a minimum power constraint. Discrete coil windings are obtained using an equi-flux streamline seeding method and are found to display an interesting spiral-type form wound on torus surfaces of elliptical cross-section. Subsequently, these results guided the design of self-shielding toroidal transverse gradient coils by While et al. [40], which display high gradient homogeneity, low inductance, high efficiency and good force balancing.

In the present paper, the 3D design method of While et al. [39] is extended to the design of 3D gradient coils for open MRI systems. Two cylindrical volumes either side of the imaging region are considered in this work and appropriate volumetric current density components are selected in terms of Fourier series. These are presented in the following section along with the corresponding field expressions of interest. In Section 3, a regularisation strategy is described for obtaining the Fourier coefficients corresponding to weighted minimum field error, minimum power and shielding constraints. A method for obtaining discrete coil windings from the volumetric current density is summarised in Section 4 along with a secondary optimisation for the coil currents. In Section 5, results are given for a variety of design considerations, and some concluding remarks are given in Section 6.

2. Model geometry and three-dimensional current density

In this section, the 3D volumetric current density representation for the open system gradient coils will be described and the corresponding expression for the induced magnetic field vector will be derived. Physical constraints on the available 3D solution space obviously include the presence of the patient imaging volume, the primary magnet and associated structures, and the requirement for the final coil set to satisfy an open configuration. To this end, two cylindrical volumes are considered of radius L, lying coaxially with the z-axis and extending from $z = a$ to $z = b$ and from $z = -a$ to $z = -b$, as depicted in Fig. 1. The upper volume car-
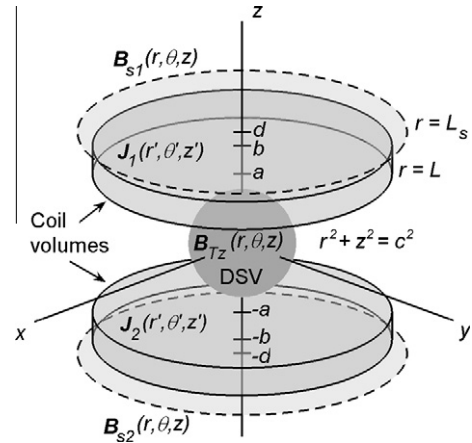

Fig. 1. The model used to describe the open 3D gradient coil: two cylindrical volumes of radius L, lying coaxially with the z-axis, extending from $z = a \rightarrow b$ and $z = -a \rightarrow -b$, and containing the 3D current densities $\mathbf{J}_1$ and $\mathbf{J}_2$. There exists a spherical interior target region (DSV) of radius c, centred at the origin, containing a desired gradient target field B_{Tz}, and two exterior circular shield target regions of radius L_s, positioned at $z = \pm d$, on which a null field is desired.

ries an unknown current density vector $\mathbf{J}_1(r', \theta', z')$ and the lower volume $\mathbf{J}_2(r', \theta', z')$ (A/m²). We intend to solve for these current densities such that they induce a linear magnetic field on a spherical target region of radius c, centred at the origin, called the diameter spherical volume (DSV). In addition, active shielding may be included in the model by also minimising the induced field on exterior circular target regions of radius L_s, centred at $z = \pm d$ (see Fig. 1).

In the present work we intend to solve for a transverse x-gradient coil, and hence as a result of the symmetry of the arrangement in Fig. 1 we may immediately put:

$$\mathbf{J}_2(r', \theta', z') = \mathbf{J}_1(r', \theta', -z'). \tag{1}$$

Note that for the case of a z-gradient coil we would instead have $\mathbf{J}_2(r', \theta', z') = -\mathbf{J}_1(r', \theta', -z')$. Fourier series are used to represent the current density components, which are chosen to be 2π-periodic in coordinate θ', $2L$-periodic in r' and $2(b-a)$-periodic in z', for generality. Boundary constraints on the current density components demand that $J_{1r}(L, \theta', z') = 0$, $J_{1z}(r', \theta', a) = J_{1z}(r', \theta', b) = 0$ and $J_1(0, \theta', z') = 0$. In addition, the three components must satisfy the time independent continuity equation:

$$\nabla \cdot \mathbf{J}_1 = 0. \tag{2}$$

Appropriate current density components were therefore chosen as follows:

$$J_{1r}(r', \theta', z') = \sum_{m=1}^{M} \sum_{k=1}^{K} m \sin\left(\frac{k\pi r'}{L}\right) [F_{m0k} \cos m\theta' + G_{m0k} \sin m\theta']$$
$$+ \sum_{n=1}^{N} \sum_{m=1}^{M} \sum_{k=1}^{K} m \left\{ \sin\left(\frac{k\pi r'}{L}\right) \cos\left(\frac{n\pi(z'-a)}{(b-a)}\right) \right.$$
$$\times [F_{mnk} \cos m\theta' + G_{mnk} \sin m\theta']$$
$$\left. + \sin\left(\frac{k\pi r'}{L}\right) \sin\left(\frac{n\pi(z'-a)}{(b-a)}\right) [P_{mnk} \cos m\theta' + Q_{mnk} \sin m\theta'] \right\}, \tag{3}$$

$$J_{1z}(r', \theta', z') = \sum_{n=1}^{N} \sum_{m=1}^{M} m \frac{r'}{L} \sin\left(\frac{n\pi(z'-a)}{(b-a)}\right) [A_{mn0} \cos m\theta' + B_{mn0} \sin m\theta']$$
$$+ \sum_{n=1}^{N} \sum_{m=1}^{M} \sum_{k=1}^{K} m \left\{ \frac{r'}{L} \cos\left(\frac{k\pi r'}{L}\right) \sin\left(\frac{n\pi(z'-a)}{(b-a)}\right) \right.$$
$$\times [A_{mnk} \cos m\theta' + B_{mnk} \sin m\theta']$$
$$\left. + \sin\left(\frac{k\pi r'}{L}\right) \sin\left(\frac{n\pi(z'-a)}{(b-a)}\right) [C_{mnk} \cos m\theta' + D_{mnk} \sin m\theta'] \right\}, \tag{4}$$

and $J_{1\theta}(r', \theta', z')$ can be obtained by enforcing Eq. (2):

$$J_{1\theta}(r', \theta', z') = -\int \left(J_{1r} + r'\frac{\partial J_{1r}}{\partial r'} + r'\frac{\partial J_{1z}}{\partial z'} \right) d\theta'. \tag{5}$$

The resultant expression for $J_{1\theta}$ is lengthy and is not shown here in interests of space. Note that we have introduced the unknown Fourier coefficients A_{mn0}, B_{mn0}, F_{m0k}, G_{m0k}, A_{mnk}, B_{mnk}, C_{mnk}, D_{mnk}, F_{mnk}, G_{mnk}, P_{mnk} and Q_{mnk} ($m = 1{:}M$, $n = 1{:}N$, $k = 1{:}K$), to be solved for later. For generality, the radial component (3) above includes $n = 0$ modes independent of the z'-coordinate and the axial component (4) includes $k = 0$ modes. Note that Bessel functions could be used to govern the radial dependence of the current density components (3)–(5); however, trigonometric functions have been chosen for convenience since these functions and their derivatives belong to an orthogonal set.

The magnetic induction vector **B**(**r**) at the field point **r** due to current density **J**(**r**') at source points **r**' (within volume V), can be calculated using the Biot–Savart law [41, p. 178]. In gradient coil operation it is the axial component of this magnetic induction vector that is important, and for the present problem this is given as follows in terms of cylindrical coordinates:

$$B_z(r, \theta, z) = -\frac{\mu_0}{4\pi} \int_a^b \int_0^{2\pi} \int_0^L h[r\sin(\theta' - \theta)J_{1r} \\ -(r' - r\cos(\theta' - \theta))J_{1\theta}]r' \, dr' \, d\theta' \, dz', \tag{6}$$

where

$$h = \frac{1}{R_-^3} + \frac{1}{R_+^3}, \tag{7}$$

and

$$R_\pm = \left[r'^2 + r^2 - 2r'r\cos(\theta' - \theta) + (z' \pm z)^2 \right]^{1/2}. \tag{8}$$

Note that since an *x*-gradient coil is being considered in this work, the symmetry argument leading to Eq. (1) has also been applied to give Eq. (6) in terms of the current density for the upper volume, $\mathbf{J}_1(r', \theta', z')$, alone. To consider a *z*-gradient coil, the second term in the expression for h in (7) would have to be subtracted from the first term rather than added; however, different Fourier series for the current density components in Eqs. (3)–(5) would also have to be considered in this case to allow $m = 0$ modes that did not involve the coordinate angle θ'.

Substituting Eq. (3) and the corresponding expression for $J_{1\theta}(r', \theta', z')$ from Eq. (5) into Eq. (6) and performing the change of variables ($\beta = \theta' - \theta$) and some trigonometric manipulation, we arrive at the following Fourier series expression for the axial component of the magnetic induction vector:

$$B_z(r, \theta, z) = \mu_0 \sum_{m=1}^M \sum_{k=1}^K U_{m0k}(r, z)[F_{m0k}\sin m\theta - G_{m0k}\cos m\theta] \\ + \mu_0 \sum_{n=1}^N \sum_{m=1}^M S_{mn0}(r, z)[A_{mn0}\sin m\theta - B_{mn0}\cos m\theta] \\ + \mu_0 \sum_{n=1}^N \sum_{m=1}^M \sum_{k=1}^K \{U_{mnk}(r, z)[F_{mnk}\sin m\theta - G_{mnk}\cos m\theta] \\ + V_{mnk}(r, z)[P_{mnk}\sin m\theta - Q_{mnk}\cos m\theta] \\ + S_{mnk}(r, z)[A_{mnk}\sin m\theta - B_{mnk}\cos m\theta] \\ + T_{mnk}(r, z)[C_{mnk}\sin m\theta - D_{mnk}\cos m\theta]\}. \tag{9}$$

Here we have introduced the following intermediate functions, for convenience:

$$U_{mnk}(r, z) = \frac{1}{2\pi} \int_a^b \int_0^\pi \int_{-L}^L hmr'r\sin\beta\sin m\beta \\ \times \sin\left(\frac{k\pi r'}{L}\right)\cos\left(\frac{n\pi(z' - a)}{(b - a)}\right)dr' \, d\beta \, dz' \\ -\frac{1}{2\pi} \int_a^b \int_0^\pi \int_{-L}^L hr'(r' - r\cos\beta)\cos m\beta \\ \times \left[\sin\left(\frac{k\pi r'}{L}\right) + \frac{k\pi r'}{L}\cos\left(\frac{k\pi r'}{L}\right)\right] \\ \times \cos\left(\frac{n\pi(z' - a)}{(b - a)}\right)dr' \, d\beta \, dz' \tag{10}$$

$$V_{mnk}(r, z) = \frac{1}{2\pi} \int_a^b \int_0^\pi \int_{-L}^L hmr'r\sin\beta\sin m\beta \\ \times \sin\left(\frac{k\pi r'}{L}\right)\sin\left(\frac{n\pi(z' - a)}{(b - a)}\right)dr' \, d\beta \, dz' \\ -\frac{1}{2\pi} \int_a^b \int_0^\pi \int_{-L}^L hr'(r' - r\cos\beta)\cos m\beta \\ \times \left[\sin\left(\frac{k\pi r'}{L}\right) + \frac{k\pi r'}{L}\cos\left(\frac{k\pi r'}{L}\right)\right] \\ \times \sin\left(\frac{n\pi(z' - a)}{(b - a)}\right)dr' \, d\beta \, dz' \tag{11}$$

$$S_{mnk}(r, z) = -\frac{1}{2\pi} \int_a^b \int_0^\pi \int_{-L}^L h\frac{n\pi}{(b - a)}\frac{r'^3}{L}(r' - r\cos\beta) \\ \times \cos m\beta\cos\left(\frac{k\pi r'}{L}\right)\cos\left(\frac{n\pi(z' - a)}{(b - a)}\right)dr' \, d\beta \, dz' \tag{12}$$

$$T_{mnk}(r, z) = -\frac{1}{2\pi} \int_a^b \int_0^\pi \int_{-L}^L h\frac{n\pi}{(b - a)}r'^2(r' - r\cos\beta) \\ \times \cos m\beta\sin\left(\frac{k\pi r'}{L}\right)\cos\left(\frac{n\pi(z' - a)}{(b - a)}\right)dr' \, d\beta \, dz' \tag{13}$$

and the function h was given previously by Eq. (7).

3. Regularisation solution process for the Fourier coefficients

The aim is to solve for the Fourier coefficients of the current density components J_{1r}, $J_{1\theta}$ and J_{1z}, such that the axial component of the magnetic induction vector closely matches some desired target field on the surface of the spherical target region called the diameter spherical volume (DSV in Fig. 1). This makes Eq. (6) a Fredholm integral equation of the first kind (see for example, [42, p. 299]), and a regularisation strategy will be described in this section for solving this highly ill-conditioned problem.

Tikhonov regularisation was first utilized in gradient coil design by Forbes and Crozier [8]. In this method, a residual error Γ is minimised with respect to the current density coefficients. For the present problem we choose a residual error of the form:

$$\Gamma = \Phi + \lambda_S\Phi_S + \lambda_P\Pi. \tag{14}$$

Here the function Φ represents the field error between the induced field B_z (9) and the target field B_{Tz} over the surface of the DSV:

$$\Phi = c \int_{-c}^c \int_{-\pi}^\pi \{[B_z(r_c, \theta, z) - B_{Tz}]^2\}d\theta \, dz, \tag{15}$$

where $r_c = \sqrt{c^2 - z^2}$. The function Φ_S in Eq. (14) represents a measure of the total magnetic flux over the surface of the exterior circular shield target regions (see Fig. 1):

$$\Phi_S = \int_{-\pi}^\pi \int_0^{L_S} \left[B_z^2(r, \theta, d) + B_z^2(r, \theta, -d) \right] r \, dr \, d\theta, \tag{16}$$

with the corresponding weight λ_S for this shielding constraint. The last term in the expression for Γ (14) involves the regularising parameter λ_P multiplied by some penalty function Π, which serves to improve the conditioning of the problem.

The choice of penalty function Π depends largely on the design criteria for the particular problem. Since a complex 3D current density vector is being considered in the present paper, we choose a penalty function that represents minimum total coil power, for simplicity:

$$\Pi = \int_a^b \int_{-\pi}^{\pi} \int_0^L \left[J_{1r}^2 + J_{1\theta}^2 + J_{1z}^2 \right] r' \, dr' \, d\theta' \, dz'. \tag{17}$$

Note that Eq. (17) could be replaced with a penalty function representing minimum inductance, coil winding curvature, or any other feature of the coil that is quadratic with respect to the current density. However, power is a common choice of constraint for gradient coil design in the pursuit of highly efficient coils and serves well here in demonstrating the overall 3D design philosophy.

Substituting Eqs. (3)–(5) and (9) appropriately into Φ in (15), Φ_S in (16) and Π in (17), and differentiating the expression for Γ in (14) with respect to the unknown current density Fourier coefficients leads to a set of linear equations in terms of these Fourier coefficients. For example, substituting Eq. (9) into Eq. (15) and differentiating with respect to F_{uvw} gives the following minimum field error condition for this coefficient:

$$\begin{aligned}
\frac{\partial \Phi}{\partial F_{uvw}} = {} & 2\pi c \mu_0^2 \sum_{k=1}^K F_{u0k} \int_{-c}^c U_{u0k}(r_c, z) U_{uvw}(r_c, z) dz \\
& + 2\pi c \mu_0^2 \sum_{n=1}^N A_{un0} \int_{-c}^c S_{un0}(r_c, z) U_{uvw}(r_c, z) dz \\
& + 2\pi c \mu_0^2 \sum_{n=1}^N \sum_{k=1}^K \left\{ F_{unk} \int_{-c}^c U_{unk}(r_c, z) U_{uvw}(r_c, z) dz \right. \\
& + P_{unk} \int_{-c}^c V_{unk}(r_c, z) U_{uvw}(r_c, z) dz \\
& + A_{unk} \int_{-c}^c S_{unk}(r_c, z) U_{uvw}(r_c, z) dz \\
& \left. + C_{unk} \int_{-c}^c T_{unk}(r_c, z) U_{uvw}(r_c, z) dz \right\} \\
& - 2c \mu_0 \int_{-c}^c \int_{-\pi}^{\pi} B_{Tz}(r_c, \theta, z) U_{uvw}(r_c, z) \sin u\theta \, d\theta \, dz.
\end{aligned} \tag{18}$$

Similar conditions exist for the remaining coefficients, and the same process is applied to Eqs. (16) and (17) to obtain shielding and minimum power conditions for each coefficient, but these are not shown here in interests of space. The integrals in the resulting expressions, such as Eq. (18), may be evaluated numerically. In this work, the trapezoidal rule was used to evaluate integrals with respect to β and θ', and Legendre–Gauss quadrature was used to evaluate integrals with respect to r, z, r' and z' [43].

The complete system of linear equations defining the coefficient conditions arising from minimising the residual error Γ in Eq. (14) can be expressed in the following matrix equation form:

$$(A + \lambda_S A_S + \lambda_P P)\mathbf{X} = \mathbf{T}. \tag{19}$$

Here matrix A (square) and vector $\mathbf{T}$ contain the minimum field error conditions arising from Eq. (15), such as Eq. (18), matrix A_S contains the shielding conditions arising from Eq. (16), matrix P contains the minimum power conditions arising from Eq. (17), and the unknown current density coefficients are stored in the vector $\mathbf{X}$ (of length $2MN + 2MK + 8MNK$). Altering the weight λ_S changes the level of shielding in the corresponding solution. Increasing the value of the regularising parameter λ_P decreases coil power and also improves the conditioning of the matrix Eq. (19) at the expense of an accurate match between the induced field and the target field. Solving Eq. (19) yields the Fourier coefficients, which can be used

in Eqs. (3)–(5) for calculating the 3D current density, and Eqs. (6) or (9) for calculating the axial component of the corresponding magnetic induction vector.

4. Obtaining 3D coil windings and calculating coil performance

Once a 3D current density solution has been obtained by solving Eq. (19), this must be discretised in some way to create corresponding 3D gradient coil windings. In this section, an approximate equi-flux streamline seeding technique will be presented for this purpose, along with the means for calculating the coil current and measures of coil performance.

In more conventional gradient coil design, in which a 2D current density (A/m) solution is obtained on some predetermined coil surface, a streamfunction exists which relates the two components of current density as a consequence of satisfying the zero divergence condition (2). Precise coil winding locations can be obtained by contouring this associated streamfunction for the 2D problem [44]. However, for the present case of a 3D current density, a single streamfunction is not available and we instead look to plot streamlines to find the locations of the coil windings for the 3D gradient coil. The problem therefore lies in choosing appropriate points at which to seed the streamlines such that they represent equal increment of current and, collectively, best approximate the 3D current density.

Many streamline seeding techniques exist for visualising 2D and 3D vector fields using evenly spaced or feature based streamlines. One method is presented by Schlemmer et al. [45] in which the density of the streamlines can be controlled by any feature of the vector field or indeed be user-defined. This method, dubbed "priority streamlines" by those authors, was adapted by While et al. [39] for calculating 3D gradient coil windings for a cylindrical whole-body scanner. More recently, this equi-flux streamline seeding method has been improved further as described in the tutorial article by While and Forbes [46] and applied successfully to a range of 1D, 2D and 3D problems by those authors. Here this method will be outlined briefly and applied to the present 3D gradient coil problem.

A scalar function $D(r', \theta', z')$ called the density map is created and chosen to be equal to the current density magnitude at all points within the coil volume:

$$D(r', \theta', z') = \left(J_{1r}^2 + J_{1\theta}^2 + J_{1z}^2 \right)^{1/2}, \tag{20}$$

into which Eqs. (3) and (4) and the corresponding expression for $J_{1\theta}(r', \theta', z')$ from Eq. (5) are substituted. The seeding point for the first streamline is chosen to correspond to the location of the maximum of this density map. This streamline is then integrated and in the present paper the inbuilt functions of the program MATLAB^TM have been used for this purpose. In cylindrical coordinates the streamline equations are as follows:

$$\frac{dr}{J_{1r}} = \frac{rd\theta}{J_{1\theta}} = \frac{dz}{J_{1z}}. \tag{21}$$

In addition, since the current density is divergence free (2), all streamlines must be closed and a check is included in the tracking algorithm to truncate the streamline once it has returned to within some small distance from the seed point (see [46]).

Once a streamline has been obtained, a 3D Gaussian filter is applied to the density map along the trace of the streamline. That is, the density map is lowered on and about the streamline, by subtracting a set of 3D Gaussian functions centred on the vertices of the streamline. Note that care must be taken to use only equi-distant streamline vertices to ensure an even filter and a simple minimum distance check stepping algorithm can be included for this purpose (see [46]). In terms of Cartesian coordinates, the Gaussian filter is of the form:

$$f(x,y,z) = A \sum_{t=1}^{T} \exp\left\{ -\left[\left(\frac{x-x_t}{\sigma}\right)^2 + \left(\frac{y-y_t}{\sigma}\right)^2 + \left(\frac{z-z_t}{\sigma}\right)^2 \right] \right\}. \tag{22}$$

Here, the points (x_t, y_t, z_t) $(t = 1:T)$ represent the reduced set of equidistant streamline vertices, (x, y, z) represents all points in the 3D volume, and the sum over t is normalized for each streamline. The amplitude A of the Gaussian filter for the entire streamline is chosen to be equal to the current maximum of the density map. The variance σ is scaled appropriately by the current maximum of the density map such that the volume integral of the filter is constant for each streamline. To this end, it can be shown that for a 3D Gaussian function the variance must scale by the inverse cube-root of the amplitude (see [46]).

Applying the Gaussian filter (22) to the density map (20) produces an updated density map and the next streamline is seeded at the location corresponding to the maximum of this new density map. The entire process is repeated continuously, whereby the density map is successively lowered with each additional streamline, until the maximum of the updated density map falls below some threshold. For 3D vector fields, an appropriate threshold was found by While and Forbes [46] to be $1/\sqrt{3}e$ times the original density map maximum and this was chosen for the present problem too. Streamline density and the total number of streamlines seeded can be controlled therefore by careful choice of the initial variance for the first streamline, and the variance for subsequent streamlines is scaled by the amplitude as described above. Clearly the final set of 3D coil windings obtained in this manner represent the 3D current density only approximately. Nevertheless, accurate solutions have been obtained for simple 1D, 2D and 3D examples using this equi-flux streamline seeding method, and the reader is directed to While and Forbes [46] for further details.

Once the coil windings have been obtained, it is important to calculate appropriate coil currents for each coil set, such that the efficiency, magnetic field and gradient homogeneity can be calculated, in addition to the coil inductance. Due to the approximate nature of the equi-flux streamline seeding method (as opposed to the exact nature of contouring a streamfunction on a 2D surface), these values are not expected to be superior to existing open gradient designs necessarily, and instead the aim of the work is to gain general insight into possible useful geometries for further optimisation. Nevertheless, these parameters are calculated to provide some benchmark values for these 3D gradient coil structures.

For two sets of W coil windings, symmetric about $z = 0$, carrying current I_w $(w = 1:W)$ and containing vertices $\left(x'_{wq}, y'_{wq}, z'_{wq}\right)$ $(q = 1:Q_w)$, the axial component of the magnetic induction vector is given by:

$$B_z(x,y,z) = \frac{\mu_0}{4\pi} \sum_{w=1}^{W} I_w \sum_{q=1}^{Q_w} \left(\frac{1}{R_{-,wq}^3} + \frac{1}{R_{+,wq}^3} \right)$$
$$\times \left[\left(x'_{wq} - x\right)\Delta y'_{wq} - \left(y'_{wq} - y\right)\Delta x'_{wq} \right], \tag{23}$$

where

$$R_{\pm,wq} = \left[\left(x'_{wq} - x\right)^2 + \left(y'_{wq} - y\right)^2 + \left(z'_{wq} \pm z\right)^2 \right]^{1/2}, \tag{24}$$

and

$$\Delta x'_{wq} = \left(x'_{w,q+1} - x'_{wq}\right)$$
$$\Delta y'_{wq} = \left(y'_{w,q+1} - y'_{wq}\right). \tag{25}$$

Ideally, the coil currents for all the windings should be the same (i.e. $I_w = I \ \forall \ w = 1:W$). To this end, the optimum fixed current I can be obtained by putting $I_w = I$ in Eq. (23), substituting this into Eq.

(15) and minimising with respect to I. This results in the following expression for I after some suitable changes of variables (to avoid potential numerical error caused by a vanishing denominator):

$$I = \frac{4\pi}{\mu_0} \frac{\int_{-c}^{c} \int_{-\pi/2}^{\pi/2} B_{Tz} F(\theta, x) d\theta \, dx}{\int_{-c}^{c} \int_{-\pi/2}^{\pi/2} [F(\theta, x)]^2 d\theta \, dx}, \tag{26}$$
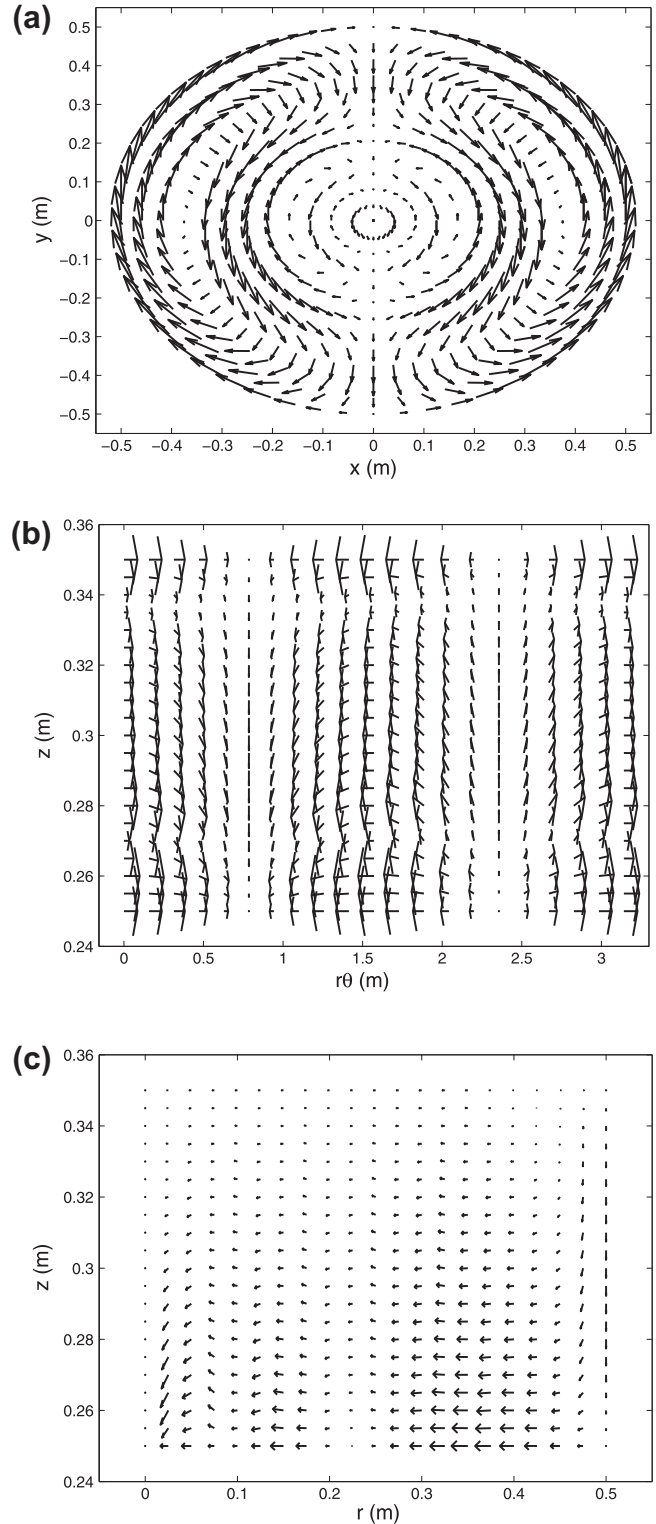

Fig. 2. Quiver plots of $\mathbf{J}_1(r', \theta', z')$ for the unshielded system, on: (a) the (x, y) plane at constant $z = a = 0.25$ m; (b) the $(r\theta, z)$ plane at constant $r = L = 0.5$ m; (c) the (r, z) plane at constant $\theta = \pi/2$ (scaled up by a factor of 4).

where

$$F(\theta,x) = \sum_{w=1}^{W} \sum_{q=1}^{Q_w} \left(\frac{1}{R_{-,wq}^3} + \frac{1}{R_{+,wq}^3} \right)$$
$$\times \left[\left(x'_{wq} - x \right) \Delta y'_{wq} - \left(y'_{wq} - \sqrt{c^2 - x^2} \sin\theta \right) \Delta x'_{wq} \right]. \quad (27)$$

However, to account for the approximate nature of the equi-flux streamline seeding method and the correspondingly approximate positions of the windings, it may be necessary to allow some variability in current across the coil winding set in the pursuit of adequate gradient homogeneity. This can be achieved by substituting Eq. (23) into Eq. (15) and minimising with respect to I_w. This yields a set of W linear equations for the coil currents I_w. However, to obtain realistic current magnitudes, these equations must be constrained and an appropriate choice of constraint is to simultaneously minimise the sum of squares of the differences between the individual coil currents and the optimum fixed coil current (26). The full set of coil currents can be obtained by solving a matrix equation of the form:

$$(D + \lambda_I I_d)\mathbf{I}_w = (\mathbf{G} + \lambda_I \mathbf{I}_f). \quad (28)$$

Here matrix D (square) and vector $\mathbf{G}$ (of length W) contain minimum field error conditions resulting from minimising Eq. (15) for the discrete case (23), matrix I_d is the identity matrix, vector $\mathbf{I}_f$ has elements equal to the optimum fixed current value (26) and the vector $\mathbf{I}_w$ contains the variable coil currents. Increasing the weighting λ_I increases the spread of current values from the optimum fixed current I (26). The solution of Eq. (28) for I_w can be used in Eq. (23) to calculate the axial component of the magnetic induction vector. Expressions for the corresponding gradient homogeneity δ (field error $= \sqrt{\delta} \times 100\%$), coil efficiency and inductance for a discrete set of windings can be found in While et al. [39], but have not been shown here in interests of space.

5. Results

In this section, 3D current density solutions for both unshielded and shielded open gradient coil sets will be presented. In addition, the corresponding 3D coil windings derived from these current densities will be displayed and discussed in terms of their general geometry and coil performance. For the open system depicted in Fig. 1, the coil volume dimensions were chosen appropriately for a whole-body arrangement with cylinder radius $L = 0.5$ m, and z-limits $a = 0.25$ m and $b = 0.35$ m. The interior target region (DSV) was chosen to be a sphere of radius $c = 0.18$ m centred at the origin.

An x-gradient with gradient strength 50 mT/m was considered, such that $B_{Tz} = 50 \times 10^{-3} r_c \cos\theta$ in Eq. (15). The outer circular shield target regions were chosen to have radius $L_s = 0.55$ m and be positioned with $d = 0.4$ m (see Fig. 1).

The program MATLAB™ was used for all instances of numerical computation. For the series expansions of the current density components (3)–(5), Fourier modes were taken to $M = 1$ and $N = K = 11$ terms, since for an x-gradient field, only the $m = 1$ mode in the Fourier series for the θ'-coordinate is necessary. Numerical integration was performed over 20 intervals to ensure convergence. The greatest computation time was associated with constructing matrix A in Eq. (19) and this took approximately 34 min on a 2 GHz Intel Core2 CPU with 2 GB of RAM.

Firstly, results for an unshielded x-gradient system will be presented. That is, the shielding weight λ_S in Eq. (19) was set to zero for this purpose. Several different values for the regularising parameter λ_P were trialled and results will be displayed for the case where $\lambda_P = 10^{-20}$. This value led to an appropriate balance between achieving a well conditioned matrix Eq. (19) and obtaining an induced gradient field of high accuracy. Increasing λ_P does improve conditioning further and results in smoother coil winding patterns and lower coil currents, however this is at the expense of field accuracy. Once the matrix Eq. (19) was solved for vector $\mathbf{X}$, the 3D current density could be computed using Eqs. (3)–(5) and the axial component of the magnetic induction vector using Eqs. (6) or (9).

Fig. 2 displays 2D quiver plots of the unshielded 3D current density $\mathbf{J}_1(r', \theta', z')$ for particular cross-sections in z, r and θ. In Fig. 2a, the quiver plot is on the (x, y) plane at constant $z = 0.25$ m, which is the inner surface of the upper volume. In this plane, the current density displays a symmetric crescent-shaped form which is similar to the current flow on the primary surfaces of traditional biplanar gradient coils (see for example, [37,38]). This crescent-shaped flow is also found at other cross-sections of constant z except that the magnitude of the current density drops as $z:a \to b$ (particularly at small r).

Fig. 2b displays a quiver plot on the $(r\theta, z)$ plane at constant $r = 0.5$ m, which is on the outer cylindrical surface of the upper volume. Note that the apparent sources and sinks of current density in this plane represent the flow of current from and to other regions of the coil volume. Similar general flow is observed at other cross-sections of constant r. Fig. 2c displays a quiver plot on the (r, z) plane at constant $\theta = \pi/2$, in which the magnitude has been scaled up by a factor of 4. Once again, similar flow is found for other cross-sections of constant θ, except with different magnitude or flow direction. The planes in Fig. 2b and c are interesting as they are
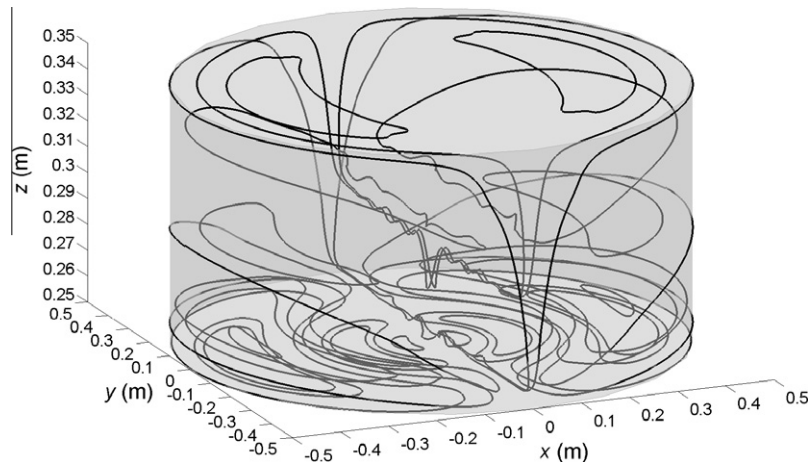

Fig. 3. 32 Coil windings used to approximate the 3D current density $\mathbf{J}_1(r', \theta', z')$ for the unshielded system (see Fig. 2), created using the equi-flux streamline seeding method.

not available in traditional biplanar gradient coil designs, in which the current is constrained to lie on planar surfaces at constant z.

The induced magnetic field corresponding to the 3D current density shown in Fig. 2 is found to display excellent gradient homogeneity with a field error of $\sqrt{\delta} = 0.15\%$ within the DSV of radius $c = 0.18$ m (or $\sqrt{\delta} = 0.04\%$ with $c = 0.15$ m). However, it is critically important to examine the discretised system of coil windings so that other measures of coil performance such as coil efficiency and inductance may be calculated. This can be achieved by applying the equi-flux streamline seeding method described briefly in Section 4 (see also, [46]). As outlined in that section, the number of coil windings can be controlled through careful choice of the initial variance for the Gaussian filter. For example, initial variances of 0.06, 0.02 and 0.01, correspond to 10, 32 and 80 coil windings, respectively, being obtained in the upper volume.

Fig. 3 displays 32 coil windings obtained using the equi-flux streamline seeding method to approximate the unshielded 3D current density of Fig. 2. Here we note that there is a concentration of coil windings on and near the inner surface at $z = a = 0.25$ m. Additional windings either have a similar form but shifted to a higher z-value, or have a portion of the winding near $x = 0$ m and $z = 0.25$ m with the return path taken far away and closer to the boundary $r = L = 0.5$ m and $z = b = 0.35$ m. This general result is perhaps expected to be optimum for a minimum power coil since it places important windings or portions of windings near the DSV and less important, or nuisance, return paths far away from this region.

Clearly the coil winding result displayed in Fig. 3 is highly complex and it is not the intention of this work that such a configuration would be physically built. Rather, these results are intended to be used to guide further optimisation on simpler coil surfaces, in a similar fashion to the toroidal coils [40] related to the original cylindrical 3D gradient coil work [39]. For example, for the minimum power case displayed in Fig. 3, an appropriate arrangement might be a flat plate on $z = a$ combined with a set of wedge or V-shaped plates of different angles and positions (aligned with y-axis) that take windings to higher z-values. However, it is important to stress that an entirely different 3D geometry may be suggested if the present method was reworked with a constraint other than coil power.

Nevertheless, we may calculate coil performance measures for the 3D coil windings as described in Section 4. For 62 coil windings the fixed current (26) is calculated to be $I = 426$ A, such that the efficiency is 117 µT/A/m. The coil inductance is found to be 585 µH for this example, such that $\eta^2/L = 23.6$ µT/A/m^4. Increasing the number of coil windings to 80 results in lower fixed current $I = 378$ A, higher efficiency 132 µT/A/m and higher inductance 901 µH ($\eta^2/L = 19.4$ µT/A/m^4). However, field error is found to be rather poor with $\sqrt{\delta} = 5.42\%$ within a DSV of radius $c = 0.15$ m (or $\sqrt{\delta} = 9.49\%$ with $c = 0.18$ m). The likely cause for this, as mentioned in Section 4, is that the equi-flux streamline seeding method only gives the approximate locations for the coil windings, which will adversely affect field quality. To account for this approximation we may allow the individual coil currents to vary slightly, by solving the matrix Eq. (28) for a particular choice of the parameter λ_I. For example, for the case of 80 coil windings, allowing the coil currents to vary by ±8% reduces the field error to $\sqrt{\delta} = 3.91\%$ within a DSV of radius $c = 0.15$ m (or $\sqrt{\delta} = 7.17\%$ with $c = 0.18$ m). A greater variance of ±25% reduces this error further to $\sqrt{\delta} = 1.67\%$ with $c = 0.15$ m (or $\sqrt{\delta} = 3.31\%$ with $c = 0.18$ m). This suggests that with more precise optimisation of this unshielded result, coil windings with high gradient homogeneity and good coil performance can be obtained.

While the results for the unshielded open 3D gradient coil in Fig. 3 are interesting, in practice it is necessary to include some level of shielding into the system. This can be achieved in the present method by selecting appropriately some finite value for the shield
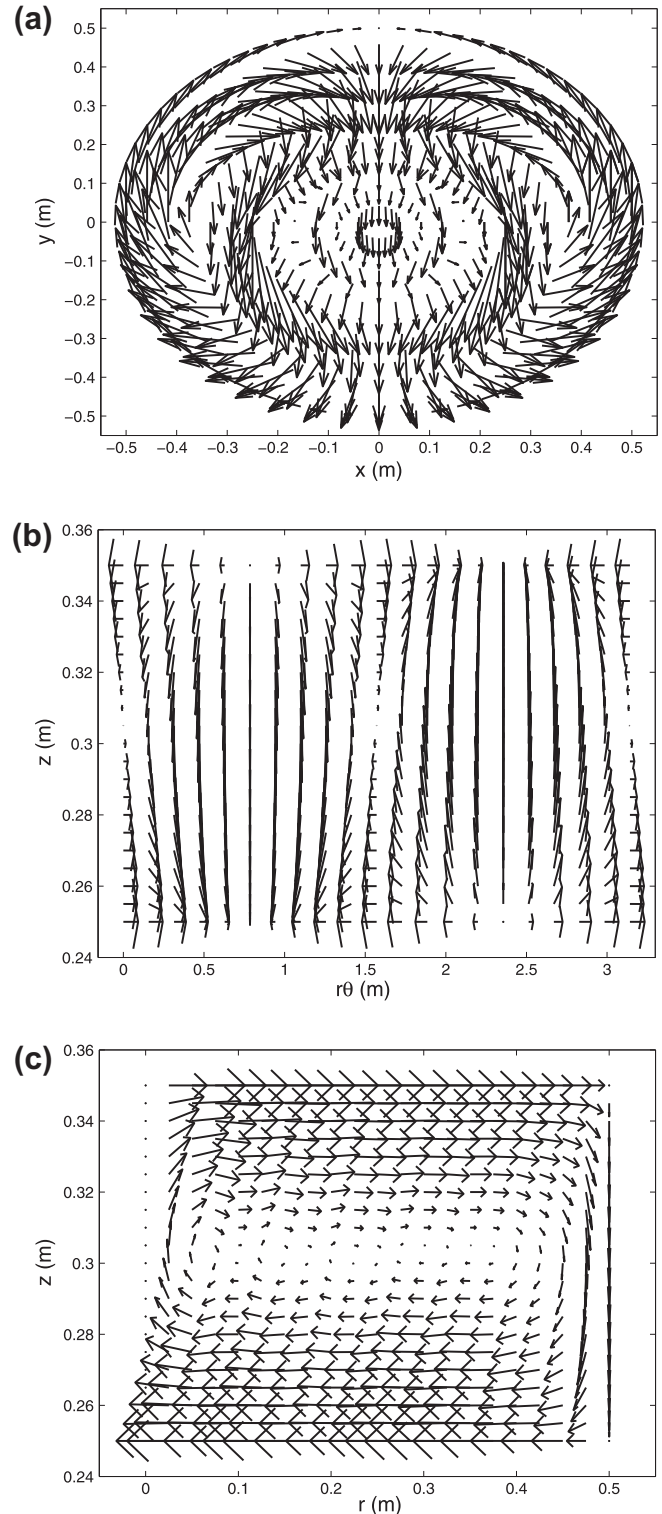

Fig. 4. Quiver plots of $\mathbf{J}_1(r', \theta', z')$ for the shielded system, on: (a) the (x, y) plane at constant $z = a = 0.25$ m; (b) the $(r\theta, z)$ plane at constant $r = L = 0.5$ m; (c) the (r, z) plane at constant $\theta = \pi/2$ (scaled up by a factor of 4).

weighting λ_S in the matrix Eq. (19). Fig. 4 displays 2D quiver plots of the shielded 3D current density $\mathbf{J}_1(r', \theta', z')$, with $\lambda_S = 10^{-4}$, for particular cross-sections in z, r and θ. In Fig. 4a, the quiver plot is on the (x, y) plane at constant $z = 0.25$ m, and the current density displays a symmetric crescent-shaped form similar to that for the unshielded result of Fig. 2a except with greater magnitude. This
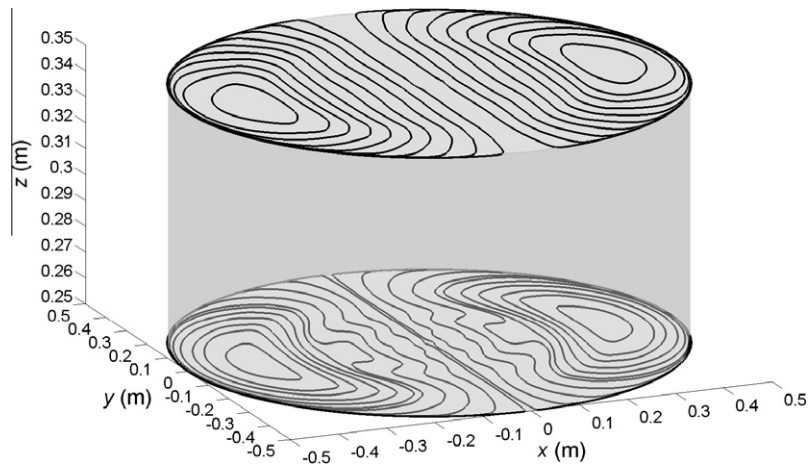
Fig. 5. 42 coil windings used to approximate the 3D current density $\mathbf{J}_1(r', \theta', z')$ for the shielded system (see Fig. 4), created using the equi-flux streamline seeding method.
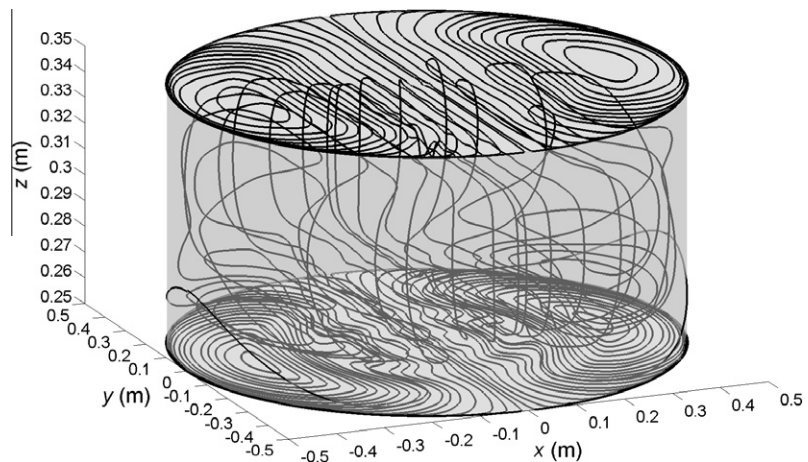

Fig. 6. 96 coil windings used to approximate the 3D current density $\mathbf{J}_1(r', \theta', z')$ for the shielded system (see Fig. 4), created using the equi-flux streamline seeding method.

crescent-shaped flow is also found at other cross-sections of constant z except that the sense of the flow reverses as $z: a \rightarrow b$.

The reversal of current direction from $z: a \rightarrow b$ is expected for the case of active shielding as the field generated by the current near $z = b$ cancels the field generated by the current near $z = a$ on the exterior circular shield target regions. As a consequence, the current density near $z = a$ must be greater in magnitude for the shielded system compared to the unshielded system, to maintain a satisfactory gradient field within the DSV, as found in Fig. 4a. The reversal of current direction is also observed in Fig. 4b, which displays a quiver plot of the shielded 3D current density on the $(r\theta, z)$ plane at constant $r = 0.5$ m, and can be compared to the unshielded equivalent in Fig. 2b. For completeness, Fig. 4c displays a quiver plot on the (r, z) plane at constant $\theta = \pi/2$, in which the magnitude has again been scaled up by a factor of 4. Note that the shielded 3D current density of Fig. 4 induces a gradient field with slightly higher field error to the unshielded system, with $\sqrt{\delta} = 0.22\%$ within a DSV of radius $c = 0.18$ m (or $\sqrt{\delta} = 0.08\%$ with $c = 0.15$ m). However, the maximum magnetic field value on the outer circular shield target region is reduced heavily by a factor of 11.

Once again, approximate coil winding locations can be obtained by applying the equi-flux streamline seeding method. Fig. 5 displays the 42 coil windings obtained for the shielded 3D current density of Fig. 4 when the initial variance for the Gaussian filter was set to 0.02. This result is remarkable and fascinating since despite having the extra degree of freedom to place windings within the coil volume, all 42 coil windings are placed exclusively on either the inner ($z = a = 0.25$ m) or outer ($z = b = 0.35$ m) coil surfaces. That is, the result almost identically matches that of a traditional biplanar x-gradient coil design (see for example, [37,38]). This suggests that for a minimum power coil, the standard biplanar configuration is already optimum with regards to overall coil geometry. Once again, this is perhaps expected since to minimise coil power it is necessary to place two sets of coil windings as close to both the DSV and shield target regions as possible.

Increasing the number of coil windings further results in some windings being placed within the coil volume. For example, Fig. 6 shows 96 coil windings obtained using the equi-flux streamline seeding method with initial variance equal to 0.01, for the shielded 3D current density of Fig. 4. These additional windings are interesting since they are self-shielding in their form. That is, they are generally aligned with the y-axis and loop from a low z-value, where they are used to induce a linear field within the DSV, to a higher z-value, where they are used to cancel the field on the shield target regions. Indeed this general form can be extended to the windings on the inner and outer surfaces. That is, to remove the difficulty of overlaying windings at $r = L = 0.5$ for both surfaces, these windings could be connected instead from $z = a$ to $z = b$ in a similar self-shielded arrangement. This configuration has previously been reported in several existing biplanar designs (see for example, [28,37,38]) and hence the present 3D result gives further credence to these established gradient coils for open systems.

As done so for the unshielded system, we may estimate field homogeneity and coil performance measures for the shielded 3D gradient coil solutions. For 70 coil windings the fixed current (26) is calculated to be $I = 924$ A, such that the efficiency is 54 μT/A/m. The coil inductance is found to be 704 μH for this example, such that $\eta^2/L = 4.2$ μT/A/m^4. Increasing the number of coil windings to 96 (see Fig. 6) results in lower fixed current $I = 587$ A, higher efficiency 85 μT/A/m and higher inductance 1569 μH ($\eta^2/L = 4.6$ μT/A/m^4). The field error for these examples is reasonable for a fixed current value and $\sqrt{\delta} < 5\%$ within a DSV of radius $c = 0.18$ m and $\sqrt{\delta} < 2.5\%$ within a DSV of radius $c = 0.15$ m. That is, for the shielded case, accounting for the approximate nature of the equi-flux streamline seeding method by allowing variation in the coil current values (by solving Eq. (28)) was unnecessary in obtaining a linear gradient field. In addition, these coil parameter estimates compare favourably with existing biplanar coil designs (see for example, [37]), despite the primary aim of the present work being to investigate optimum geometries for open system gradient coils for further precise coil winding optimisation.

6. Conclusion

A theoretical design method has been presented for obtaining 3D gradient coils for an open MRI system. A Tikhonov regularisation scheme was used to solve for the Fourier coefficients of a 3D current density vector in two cylindrical volumes either side of the imaging region. The method incorporated a minimum power constraint and allowed the inclusion of active shielding into the system. The corresponding discretised system of 3D coil windings was obtained approximately using an equi-flux streamline seeding method.

For the unshielded case, the coil windings were found to be concentrated on the inner surfaces of the coil volumes and displayed an interesting looped structure that took unwanted return path portions far away from the DSV. However, for the shielded case, the coil windings were found to lie almost exclusively on the inner and outer surfaces of the coil volumes in the arrangement of a traditional biplanar design, with additional windings displaying an inherent self-shielding property in line with recent gradient coil designs. This result suggests that existing biplanar designs are already optimum for open systems, at least with regards to minimising coil power.

The 3D design method can be adapted in a straightforward manner to consider other types of coil volumes as has been done so previously for cylindrical whole-body systems. In addition, constraints other than coil power may be incorporated easily into the design method to investigate alternative optimum 3D geometries.

References

[1] J. Jin, Electromagnetic Analysis and Design in Magnetic Resonance Imaging, CRC Press, Florida, 1999.
[2] R. Turner, Gradient coil design – a review of methods, Magnetic Resonance Imaging 11 (7) (1993) 903–920.
[3] B.L.W. Chapman, Gradients: the heart of the MRI machine, Current Medical Imaging Reviews 2 (1) (2006) 131–138.
[4] R. Turner, A target field approach to optimal coil design, Journal of Physics D – Applied Physics 19 (8) (1986) L147–L151.
[5] R. Turner, Minimum inductance coils, Journal of Physics E – Scientific Instruments 21 (10) (1988) 948–952.
[6] B.A. Chronik, B.K. Rutt, Constrained length minimum inductance gradient coil design, Magnetic Resonance in Medicine 39 (2) (1998) 270–278.
[7] J.W. Carlson, K.A. Derby, K.C. Hawryszko, M. Weideman, Design and evaluation of shielded gradient coils, Magnetic Resonance in Medicine 26 (2) (1992) 191–206.
[8] L.K. Forbes, S. Crozier, A novel target-field method for finite-length magnetic resonance shim coils: I. Zonal shims, Journal of Physics D – Applied Physics 34 (24) (2001) 3447–3455.
[9] L.K. Forbes, S. Crozier, A novel target-field method for finite-length magnetic resonance shim coils: II. Tesseral shims, Journal of Physics D – Applied Physics 35 (9) (2002) 839–849.
[10] L.K. Forbes, S. Crozier, A novel target-field method for magnetic resonance shim coils: III. Shielded zonal and tesseral coils, Journal of Physics D – Applied Physics 36 (2) (2003) 68–80.
[11] P. Verheyden, S. Katscher, T. Schulz, F. Schmidt, C. Josten, Open MR imaging in spine surgery: experimental investigations and first clinical experiences, European Spine Journal 8 (5) (1999) 346–353.
[12] J. Kettenbach, D.F. Kacher, S.K. Koskinen, S.G. Silverman, A. Nabavi, D. Gering, C.M.C. Tempany, R.B. Schwartz, R. Kikinis, P.M. Black, F.A. Jolesz, Interventional and intraoperative magnetic resonance imaging, Annual Review of Biomedical Engineering 2 (2000) 661–690.
[13] K. Yoda, Analytical design method of self-shielded planar coils, Journal of Applied Physics 67 (9, Part 1) (1990) 4349–4353.
[14] E.D. Caparelli, D. Tomasi, H. Panepucci, Shielded biplanar gradient coil design, Journal of Magnetic Resonance Imaging 9 (5) (1999) 725–731.
[15] M.A. Martens, L.S. Petropoulos, R.W. Brown, J.H. Andrews, M.A. Morich, J.L. Patrick, Insertable biplanar gradient coils for magnetic-resonance-imaging, Review of Scientific Instruments 62 (11) (1991) 2639–2645.
[16] H.Y. Liu, C.L. Truwit, True energy-minimal and finite-size biplanar gradient coil design for MRI, IEEE Transactions on Medical Imaging 17 (5) (1998) 826–830.
[17] L.K. Forbes, S. Crozier, Novel target-field method for designing shielded biplanar shim and gradient coils, IEEE Transactions on Magnetics 40 (4, Part 1) (2004) 1929–1938, doi:10.1109/TMAG.2004.828934.
[18] L.K. Forbes, M.A. Brideson, S. Crozier, A target-field method to design circular biplanar coils for asymmetric shim and gradient fields, IEEE Transactions on Magnetics 4 (6) (2005) 2134–2144, doi:10.1109/TMAG.2005.847638.
[19] W. Liu, X. Tang, D. Zu, A novel target-field approach to design bi-planar shim coils for permanent-magnet MRI, Concepts in Magnetic Resonance Part B – Magnetic Resonance Engineering 37B (1) (2010) 29–38, doi:10.1002/cmr.b.20153.
[20] S. Crozier, L.K. Forbes, D.M. Doddrell, The design of transverse gradient coils of restricted length by simulated annealing, Journal of Magnetic Resonance Series A 107 (1) (1994) 126–128.
[21] M. Zhu, L. Xia, F. Liu, S. Crozier, Deformation-space method for the design of biplanar transverse gradient coils in open MRI systems, IEEE Transactions on Magnetics 44 (8) (2008) 2035–2041, doi:10.1109/TMAG.2008.923898.
[22] D. Tomasi, Optimization of biplanar gradient coils for magnetic resonance imaging, Brazilian Journal of Physics A 36 (1) (2006) 23–27.
[23] S. Pissanetzky, Minimum energy MRI gradient coils of general geometry, Measurement Science and Technology 3 (7) (1992) 667–673.
[24] A. Ersahin, M.J. Bronskill, R.M. Henkelman, B. Collick, R.S. Hinks, Gradient coil design considerations for iron core interventional magnets, Journal of Magnetic Resonance Imaging 8 (5) (1998) 1145–1153.
[25] R.A. Lemdiasov, R. Ludwig, A stream function method for gradient coil design, Concepts in Magnetic Resonance Part B – Magnetic Resonance Engineering 26B (1) (2005) 67–80, doi:10.1002/cmr.b.20040.
[26] L. Marin, H. Power, R.W. Bowtell, C.C. Sanchez, A.A. Becker, P. Glover, A. Jones, Boundary element method for an inverse problem in magnetic resonance imaging gradient coils, Computer Modeling in Engineering and Sciences 23 (3) (2008) 149–173.
[27] M. Poole, R. Bowtell, Novel gradient coils designed using a boundary element method, Concepts in Magnetic Resonance Part B – Magnetic Resonance Engineering 31B (3) (2007) 162–175, doi:10.1002/cmr.b.20091.
[28] H.S. Lopez, M. Poole, S. Crozier, An improved equivalent magnetization current method applied to the design of local breast gradient coils, Journal of Magnetic Resonance 199 (1) (2009) 48–55, doi:10.1016/j.jmr.2009.03.011.
[29] A. Trakic, F. Liu, H.S. Lopez, H. Wang, S. Crozier, Longitudinal gradient coil optimization in the presence of transient eddy currents, Magnetic Resonance in Medicine 5 (6) (2007) 1119–1130, doi:10.1002/mrm.21243.
[30] R. Bowtell, A. Peters, Analytic approach to the design of transverse gradient coils with co-axial return paths, Magnetic Resonance in Medicine 41 (3) (1999) 600–608.
[31] B. Haywood, B. Chapman, P. Mansfield, Model gradient coil employing active acoustic control for MRI, Magnetic Resonance Materials in Physics Biology and Medicine 20 (5-6) (2007) 223–231, doi:10.1007/s10334-007-0086-y.
[32] P. Mansfield, B. Haywood, Controlled E-field gradient coils for MRI, Physics in Medicine and Biology 53 (7) (2008) 1811–1827, doi:10.1088/0031-9155/53/7/001.
[33] H. Sanchez, F. Liu, A. Trakic, E. Weber, S. Crozier, Three-dimensional gradient coil structures for magnetic resonance imaging designed using-fuzzy membership functions, IEEE Transactions on Magnetics 43 (9, Part 1) (2007) 3558–3566, doi:10.1109/TMAG.2007.902065.
[34] B.L.W. Chapman, P. Mansfield, Quiet gradient coils – active acoustically and magnetically screened distributed transverse gradient designs, Measurement Science and Technology 6 (4) (1995) 349–354.
[35] R. Kimmlingen, M. Gebhardt, J. Schuster, M. Brand, F. Schmitt, A. Haase, Gradient system providing continuously variable field characteristics, Magnetic Resonance in Medicine 47 (4) (2002) 800–808, doi:10.1002/mrm.10129.
[36] S. Shvartsman, M. Morich, G. Demeester, Z. Zhai, Ultrashort shielded gradient coil design with 3D geometry, Concepts in Magnetic Resonance Part B – Magnetic Resonance Engineering 26B (1) (2005) 1–15, doi:10.1002/cmr.b.20044.
[37] M.G. Sementchenko, Gradient coils for magnetic resonance meeting, November 2000.

[38] J.A. Overweg, Vertical field type MRI apparatus with a conical gradient coil situated in the main magnet, September 2003.

[39] P.T. While, L.K. Forbes, S. Crozier, 3-D gradient coil design-initial theoretical framework, IEEE Transactions on Biomedical Engineering 56 (4) (2009) 1169–1183, doi:10.1109/TBME.2009.2013199.

[40] P.T. While, L.K. Forbes, S. Crozier, 3D Gradient coil design – toroidal surfaces, Journal of Magnetic Resonance 198 (1) (2009) 31–40, doi:10.1016/j.jmr.2009.01.006.

[41] J.D. Jackson, Classical Electrodynamics, third ed., John Wiley & Sons, Inc., New York, 1999.

[42] L.M. Delves, J.L. Mohamed, Computational Methods for Integral Equations, Cambridge University Press, Cambridge, UK, 1985.

[43] G. von Winckel, Legendre–Gauss Quadrature Weights and Nodes, MATLAB Central File Exchange, February 2004. <http://www.mathworks.com/matlabcentral/fileexchange/4540>.

[44] M.A. Brideson, L.K. Forbes, S. Crozier, Determining complicated winding patterns for shim coils using stream functions and the target-field method, Concepts in Magnetic Resonance 14 (1) (2002) 9–18.

[45] M. Schlemmer, I. Hotz, B. Hamann, F. Morr, H. Hagen, Priority streamlines: a context-based visualization of flow fields, in: Proceedings of the Eurographics/IEEE-VGTC Symposium on Visualization, 2007, pp. 1–8.

[46] P.T. While, L.K. Forbes, Equi-flux streamline seeding for three-dimensional vector fields, IEEE Transactions on Visualization and Computer Graphics, submitted for publication.